Direct determination of band-gap renormalization in degenerately doped ultrawide band gap β-Ga_2O_3 semiconductor

Jiaye Zhang,[1,2,*] Joe Willis,[3,4,5,*] Zhenni Yang,[1] Ziqian Sheng,[1] Lai-Sen Wang,[6] Tien-Lin Lee,[5] Lang Chen,[2] David O. Scanlon,[3,4,†] and Kelvin H. L. Zhang[1,‡]

[1]*State Key Laboratory of Physical Chemistry of Solid Surfaces, College of Chemistry and Chemical Engineering, Xiamen University, Xiamen 361005, People's Republic of China*

[2]*Department of Physics, Southern University of Science and Technology, Shenzhen, Guangdong 518055, China*

[3]*Department of Chemistry, University College London, 20 Gordon Street, London WC1H 0AJ, United Kingdom*

[4]*Thomas Young Centre, University College London, Gower Street, London WC1E 6BT, United Kingdom*

[5]*Diamond Light Source Ltd., Harwell Science and Innovation Campus, Didcot OX11 0DE, United Kingdom*

[6]*Fujian Key Laboratory of Materials Genome, College of Materials, Xiamen University, Xiamen 361005, People's Republic of China*

(Received 29 April 2022; revised 3 September 2022; accepted 20 October 2022; published 21 November 2022)

Ga_2O_3 is emerging as a promising wide band-gap semiconductor for high-power electronics and deep ultraviolet optoelectronics. It is highly desirable to dope it with controllable carrier concentrations for different device applications. This work reports a combined photoemission spectroscopy and theoretical calculation study on the electronic structure of Si doped Ga_2O_3 films with carrier concentration varying from 4.6×10^{18} cm^{-3} to 2.6×10^{20} cm^{-3}. Hard x-ray photoelectron spectroscopy was used to directly measure the widening of the band gap as a result of occupation of conduction band and band-gap renormalization associated with many-body interactions. A large band-gap renormalization of 0.3 eV was directly observed in heavily doped Ga_2O_3. Supplemented with hybrid density functional theory calculations, we demonstrated that the band-gap renormalization results from the decrease in energy of the conduction band edge driven by the mutual electrostatic interaction between added electrons. Moreover, our work reveals that Si is a superior dopant over Ge and Sn, because Si 3*s* forms a resonant donor state above the conduction band minimum, leaving the host conduction band mostly unperturbed and a high mobility is maintained though the doping level is high. Insights of the present work have significant implications in doping optimization of Ga_2O_3 and realization of optoelectronic devices.

DOI: 10.1103/PhysRevB.106.205305

Ga_2O_3 is emerging as a promising wide band-gap semiconductor for high-power electronics, solar-blind deep ultraviolet (UV) photodetectors, and deep UV transparent conductive oxides (TCOs), because of its ultralarge band gap of 4.8 eV, high theoretical breakdown field of 8 MV/cm, along with the availability of large-scale substrate wafers [1–3]. These advantages offer a competitive edge over current wide band-gap semiconductors such as SiC and GaN. For the aforementioned optoelectronic device applications, precise control over the carrier concentration and defects is of essential importance. For Ga_2O_3 used as channel semiconductor in high-power electronics, a low carrier concentration less than 10^{16} cm^{-3} and minimal defects are necessary in order to achieve a high breakdown voltage [4], whereas a highly conductive layer with carrier concentrations over 10^{19} cm^{-3} is needed for Ga_2O_3 used as deep UV transparent conductive electrodes and as low-resistance Ohmic contact layers for high electron mobility transistors [5]. The technological importance of *n*-type doped Ga_2O_3 has prompted a number of studies. Group 14 elements including Si [6–8], Ge [9,10], and Sn [9,11] have been demonstrated as shallow dopants in Ga_2O_3 bulk crystals and thin films with carrier concentrations tuned in the range 10^{16}–10^{20} cm^{-3}.

On the other hand, degenerate doping of semiconductors also alters the fundamental optical and electronic structure of the host semiconductors, owing to the high concentration of free electrons and dopant ions. There has been significant interest in understanding how degenerate doping may influence the electronic structure of the technologically important wide band-gap semiconductors such as GaN [12], In_2O_3 [13,14], and $BaSnO_3$ [15], semiconductor quantum wells [16,17] as well as the emerging two-dimensional transition metal dichalcogenides [18–20]. Above the critical Mott carrier density, degenerate *n*-type doping often results in a widening of the optical band gap (E_{opt}), because of the occupation of the electronic states at the bottom of conduction band (CB) by doped electrons, i.e., Burstein-Moss shift (ΔBM). However, the widening of E_{opt} is further counteracted by band-gap shrinkage or renormalization (ΔRN), which is caused by the lowering of the CB and an upward shift of the valence band (VB) as a result of mutual exchange and Coulomb interactions between the electrons in the CB and electron-dopant interactions [21]. Therefore, the net change in optical band gap, ΔE_{opt}, can be taken as a difference of the two contributions, i.e., $\Delta E_{opt} = \Delta\text{BM} - \Delta\text{RN}$. The onset

*These authors contributed equally to this work.
†d.scanlon@ucl.ac.uk
‡Kelvinzhang@xmu.edu.cn

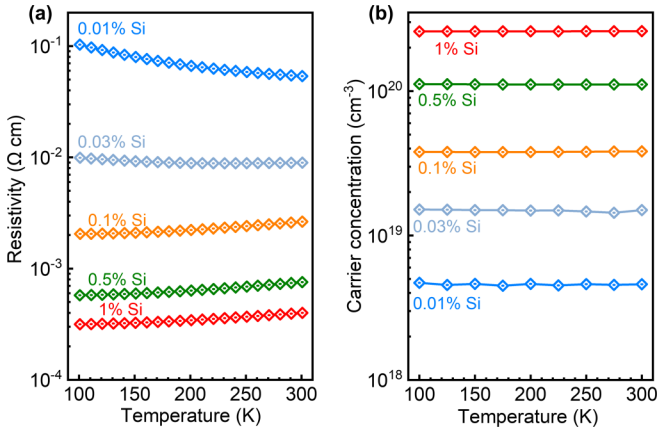

FIG. 1. Temperature dependence of (a) resistivity, and (b) carrier concentration for the $(Si_xGa_{1-x})_2O_3$ films with different x.

of E_{opt} measured using optical methods is therefore the superposition of both ΔBM and ΔRN, making it challenging to extract the respective contribution of ΔBM and ΔRN. Furthermore, although Si, Ge, and Sn have been used as donors in Ga_2O_3, it is still unclear how the electronic states of the dopants alter the band structure of host Ga_2O_3, which fundamentally determines the electron effective mass and transport properties of charge carriers [13,22,23]. Therefore, knowledge of the doping effects on optical band gap and electronic structure is crucial in selecting and improving materials for optoelectronic devices.

In this work, we report a combined photoemission spectroscopy and theoretical calculation study on the electronic structures of Si doped β-phase Ga_2O_3 thin films. Hard x-ray photoemission spectroscopy (HAXPES) was used to measure the evolution of electronic structures, which enables a direct observation of the doped electrons in the CB and an accurate measurement of the position of the CB and VB edges relative to the Fermi energy (E_F). These allowed us to explicitly disentangle the respective contributions of the ΔBM and ΔRN, which were further compared to hybrid density functional theory (DFT) calculations. A band-gap widening of ΔBM = 0.5 eV and band-gap shrinkage of ΔRN = 0.3 eV are explicitly determined for highly Si doped Ga_2O_3. Moreover, our results also reveal that Si 3*s* forms a resonant donor state above the CB minimum, leaving the host CB mostly unperturbed and a high mobility is maintained while the doping level is high, making Si a superior dopant for Ga_2O_3 over other dopants, e.g., Ge and Sn.

Si doped β-phase Ga_2O_3 ($Si_{2x}Ga_{2-2x}O_3$) thin films with Si doping levels of $x = 0.01\%$ to 1% were grown on insulating Fe doped Ga_2O_3 (010) substrates using pulsed laser deposition (PLD). All the film thickness is ~200 nm. Details for the film growth and characterizations are provided in Appendix A. Figures 1(a) and 1(b) show the temperature-dependent resistivity and carrier concentration of the Si doped films, respectively. Table I summarizes the room-temperature carrier concentration and mobility. The 1% Si doped film has the highest carrier concentration of 2.6×10^{20} cm^{-3} and a mobility of 60.5 cm^2/V s. The 0.01% Si doped film with a carrier concentration of 4.6×10^{18} cm^{-3} exhibits semiconducting behavior, whereas the Si doped films with $x > 0.03\%$ show metallic transport behavior, indicating the degenerate doping of Ga_2O_3.

TABLE I. Room-temperature carrier concentration (n_e), mobility (μ), and conductivity (σ) for the $(Si_xGa_{1-x})_2O_3$ films with different x.

Dopant	x	n_e (cm^{-3})	μ (cm^2/V s)	σ (S/cm)
Si	0.01%	4.6×10^{18}	20.7	18.6
	0.03%	1.5×10^{19}	47.5	111
	0.1%	3.8×10^{19}	62.1	378
	0.5%	1.1×10^{20}	75.0	1322
	1%	2.6×10^{20}	60.5	2500

The CB, VB, and core-level HAXPES of the Si doped Ga_2O_3 films were measured with photon energy of 5920 eV, as shown in Figs. 2 and 3. As shown in Fig. 2(a), the VB spectra of Ga_2O_3 consist of features of I, II, and III, which are assigned to the occupied O $2p^6$ states with mixture of Ga $3d$(I), $4p$ (II), and $4s$ (III) states, respectively. The CB is mainly derived from Ga $4s$ orbitals [24]. Compared to conventional XPS, HAXPES has relatively larger photoionization cross section for Ga $4s$ relative to O $2p$ [25]. This enables the direct observation of the occupied electronic states at the bottom of the CB. Figure 2(b) shows the magnified view of the filled Ga $4s$ derived CB states and the top region of VB. No appreciable CB feature is observed for the 0.01% Si doped Ga_2O_3, because its carrier density is close to the threshold for degenerate doping [2]. For Si doping level $x \geqslant 0.03\%$, a well-defined CB feature straddling the E_F, whose intensity increases with doping, is observed. This is associated with the filling of the lower CB states by degenerately doped electrons, in accordance with the metallic transport property.

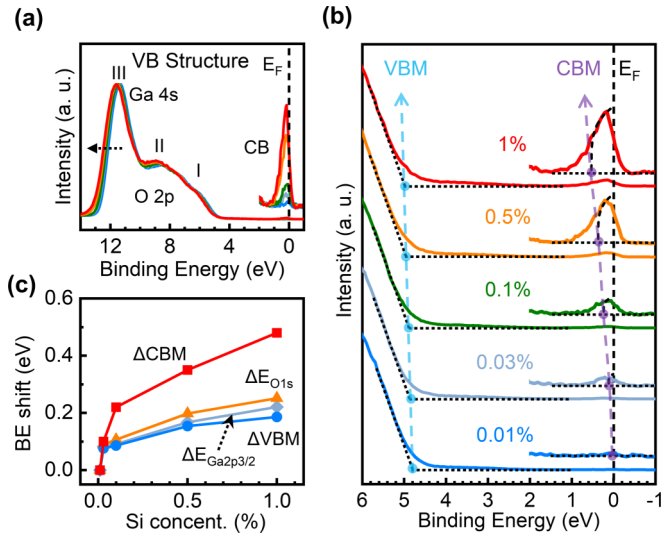

FIG. 2. (a) HAXPES measured VB and expanded view (×70) of the CB state for $(Si_xGa_{1-x})_2O_3$ with different x. (b) Expanded view of VB edge (×5) and CB feature (×50), where the VBM and CBM positions are indicated by cyan and purple dashed lines, respectively. (c) The binding energy (BE) shifts of Ga $2p_{3/2}$ ($\Delta E_{Ga2p3/2}$) and O $1s$ (ΔE_{O1s}), ΔVBM and ΔCBM with respect to the $x = 0.01\%$ sample.

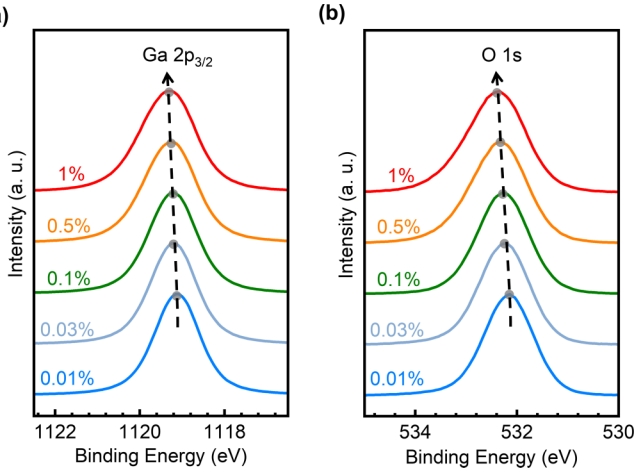

FIG. 3. (a) Ga $2p_{3/2}$ and (b) O 1s core-level spectra for $(Si_xGa_{1-x})_2O_3$ with different x, where core-level peak positions (the center of the full width at half maximum) are indicated by gray points and the dashed lines with arrow are guides to the eyes.

Figures 3(a) and 3(b) show the Ga $2p_{3/2}$ and O 1s spectra, respectively. It can be seen that both the Ga $2p_{3/2}$ and O 1s concurrently shift towards the higher BE values, because of the upshift of the E_F resulting from the filling of bottom of the CB.

One unique aspect of this study is that we can concurrently probe the positions of the CB minimum (CBM) and the VB maximum (VBM). The position of the CBM, E_{CBM}, can be fitted by $a * (E_{CBM}\text{-}E)^{1/4}$ to the feature of the CB states, where a is constant. This function represents the dominant energy term in the CB density-of-states (DOS) function and is expected to remove the influence of peak tail or plasmon satellite at high binding energy (BE) side [26,27]. The detailed procedure for extrapolating the VBM and fitting the CBM can be found in Appendix B. For the 0.01% Si doped film, the E_F is very close to the CBM. We therefore take the 0.01% film as reference. The relative BE shifts of the CBM, VBM, and core levels with respect to the 0.01% sample are plotted in Fig. 2(c). The BE for the CBM of the 1% Si film shifts (ΔCBM) by ∼0.5 eV towards higher BE. However, the BE shifts of VBM (ΔVBM) as well as the Ga $2p(\Delta E_{Ga2p3/2})$ and O $1s(\Delta E_{O1s})$ core levels with respect to those of 0.01% film, e.g., ∼0.20 eV for 1%, are much smaller than the ΔCBM [Fig. 2(c)]. The discrepancy in the BE shifts is a clear indication of band-gap renormalization resulting from electron-electron or electron-dopant interactions when the doping level is high.

The band filling and band-gap renormalization are further qualitatively modeled using semiconductor carrier statistics. As shown in Fig. 4(a), for a direct band-gap degenerate semiconductor, the measured energy separation between VBM and E_F (denoted as E_F−VBM) in HAXPES reflects the onset of E_{opt}, and the separation between the VBM and CBM corresponds to the fundamental band gap (E_g). Therefore, the measured difference of E_F−VBM (ΔVBM) corresponds to the net change in optical band gap, $\Delta E_{opt} = \Delta BM - \Delta RN$, while the measured difference between the shifts of CBM and VBM corresponds to the value of band-gap renormalization (ΔRN), i.e., ΔRN = ΔCBM − ΔVBM. Figure 4(b)

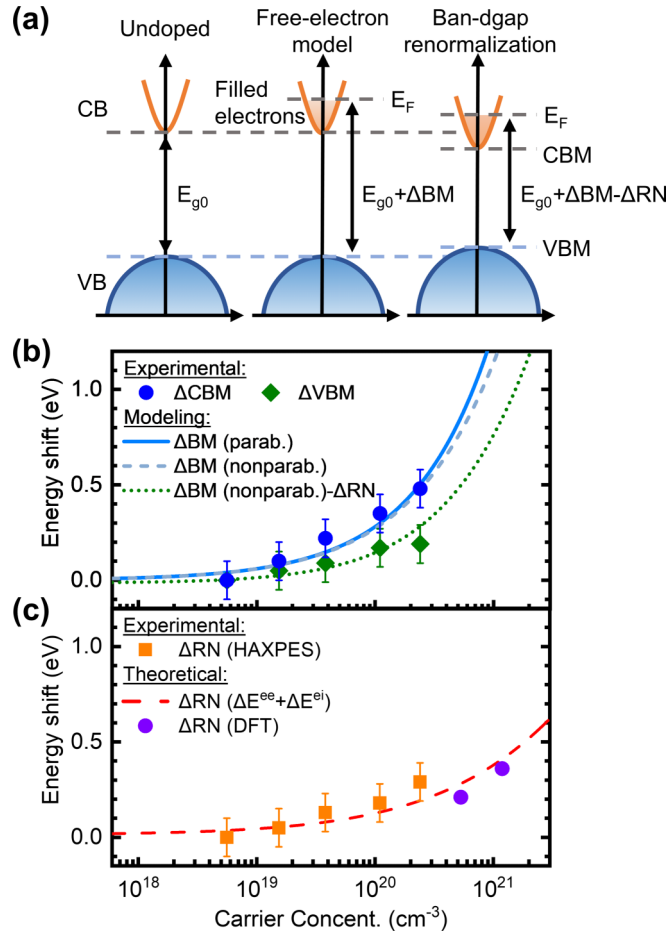

FIG. 4. (a) Schematic diagram for change of the electron structure for Si doped Ga_2O_3. Degenerate doping gives rise to an increase of optical band gap ($E_{opt} = E_{g0} + \Delta BM$) by Burstein-Moss shift (ΔBM) due to the occupation of bottom of CB (middle panel). However, the widening of E_{opt} is further counteracted by band-gap renormalization (ΔRN) (right panel). (b) Carrier concentration dependent ΔBM obtained from parabolic [ΔBM (parab.)] and nonparabolic [ΔBM (nonparab.)] Burstein-Moss model without and with consideration of ΔRN [ΔBM (nonparab.)-ΔRN], as well as HAXPES measured ΔVBM and ΔCBM. (c) The carrier concentration dependent ΔRN obtained from HAXPES [ΔRN (HAXPES)], semiconductor statistics modeling [$\Delta RN(\Delta E^{ee} + \Delta E^{ei})$] and DFT calculation [ΔRN (DFT)].

plots the HAXPES measured ΔVBM (green diamonds) and ΔCBM (blue circles) as a function of carrier concentrations. The experimental data are compared to the carrier statistics using parabolic and nonparabolic models with and without consideration of band-gap renormalization (the procedure for simulation of carrier statistics is provided in Appendix C). It can be seen from Fig. 4(b) that the measured ΔCBM as the function of carrier concentrations agrees well with both parabolic and nonparabolic models, consistent with the rigid band filling of electrons at the CB. However, the measured ΔVBM (green diamonds) is much smaller than values predicted by both models. Band-gap renormalization, therefore, should be considered. The measured ΔRN values are shown by orange squares in Fig. 4(c), e.g., the measured ΔRN for the 1% doped film is ∼0.3 eV.

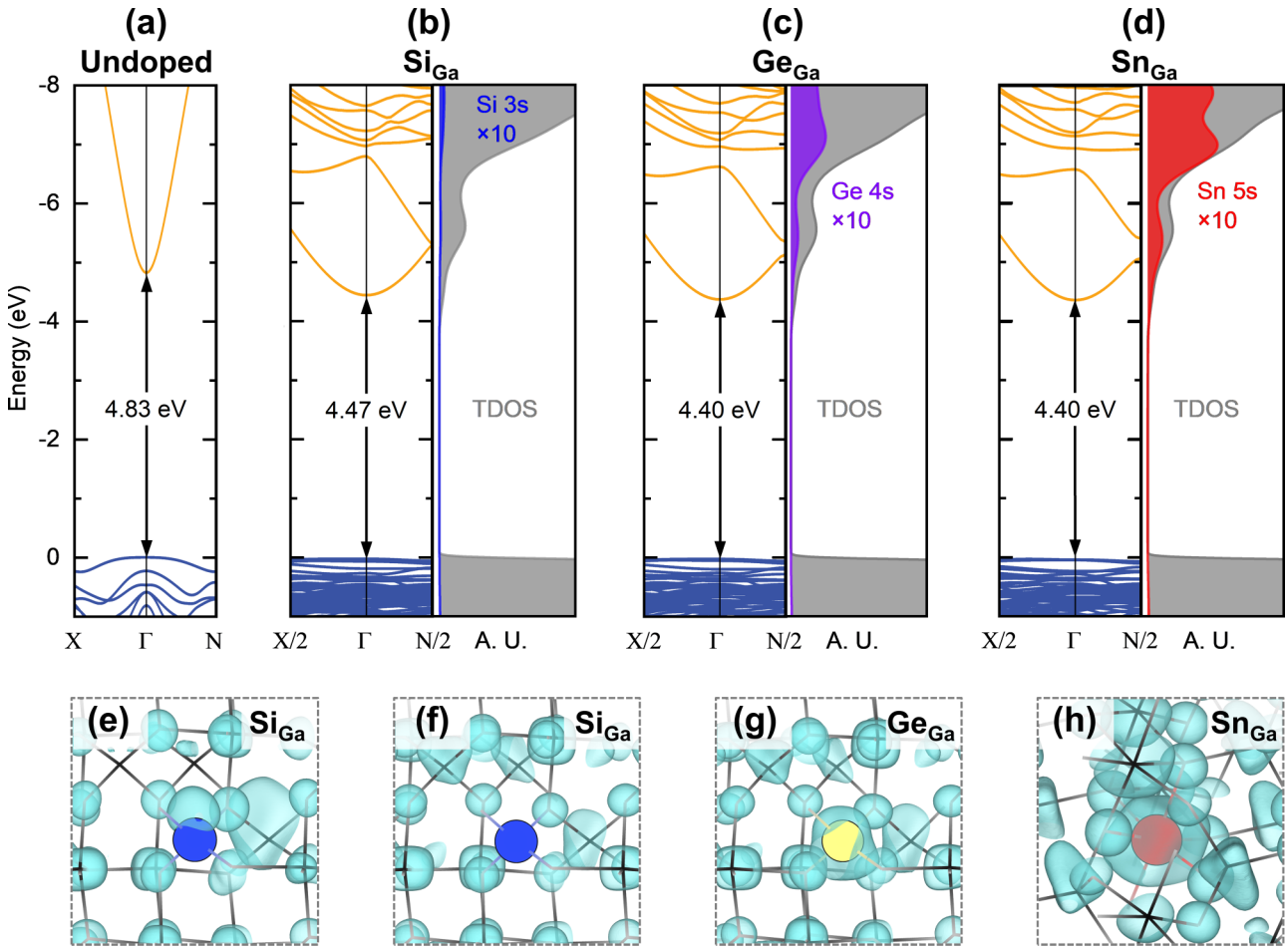

FIG. 5. (a)–(d) Hybrid DFT calculated band structure and total (TDOS) and partial density of states (PDOS) for (a) ten-atom undoped Ga_2O_3 primitive unit cell and (b) Si, (c) Ge, and (d) Sn doped 80-atom supercells, in which the PDOS for dopant *s* state are magnified (×10) for clarity and the top of the VBM is set to zero energy. (e)–(h) The partial charge densities (e) at the defect states localized at ∼2 eV above the CBM of Ga_2O_3 for Si_{Ga}, as well as at the CBM of Ga_2O_3 for (f) Si_{Ga}, (g) Ge_{Ga}, and (h) Sn_{Ga}, which are plotted with an isosurface density of 0.007 electrons per $Å^{-3}$.

Both the electron-electron interaction (ΔE_g^{ee}) and electron-impurity interaction (ΔE_g^{ei}) are expected to induce band-gap renormalization ($\Delta RN = E_g^{ee} + \Delta E_g^{ei}$) and compensate the ΔBM [21]. By taking the contribution of ΔRN into account, the modeled ΔBM (nonparab.)-ΔRN [Fig. 4(b) (green dashed line)] agrees well with the HAXPES measured ΔVBM. Furthermore, the modeled ΔRN also reproduces well the measured ΔRN [Fig. 4(c)]. It should be noted that the modeled ΔRN presented here is only based on the electrostatic interaction model without considering the orbital hybridization of Si dopant with the host CB.

Hybrid DFT calculations were carried out to further examine the electronic structure. Figure 5(a) shows the calculated band structure for undoped Ga_2O_3 with a ten-atom unit cell. The calculated band structures for 1 Si dopant in an 80- and 180-atom supercell, corresponding to a carrier concentration of 1.1×10^{21} cm^{-3} and 5.3×10^{20} cm^{-3}, respectively, are shown in Figs. 5(b) and Appendix D. The calculated results show that the band gap is reduced from 4.83 eV for undoped Ga_2O_3 [Fig. 5(a)] to 4.62 eV (5.3×10^{20} cm^{-3}) (Appendix D) and 4.47 eV (1.1×10^{21} cm^{-3}) for doped Ga_2O_3 [Fig. 5(b)]. The band-gap reduction is mainly caused by the downshift of CB edge, because of the highly dispersive Ga 4*s* derived CB, while the VB edge is flat and with a large effective mass. As shown in Fig. 4(c), the calculated ΔRN (purple circles) agrees well with the modeled ΔRN based on the electrostatic interaction model. We expect that the renormalization effect should be more pronounced in the modulated doped 2DEG at $(Al_xGa_{1-x})_2O_3/Ga_2O_3$ interface, because of the enhanced Coulomb interaction at the quantum well [16,17,28], which may have important implications for high mobility transistor application.

Interestingly, we find that the Si 3*s* forms a resonant donor state sitting at ∼2 eV above the CBM and can easily donate the extra electrons to the host CB [Fig. 5(b)]. There is very little hybridization between the Si 3*s* state and the Ga 4*s* derived host CBM, leaving the CBM relatively unperturbed, even when the doping level is high. Therefore, the band-gap renormalization observed in Si doped Ga_2O_3 mainly arises from a high density of free electrons induced many-body exchange interactions. This is different from other widely used oxide semiconductors, such as Sb doped SnO_2 [22] and

Sn doped In_2O_3 [23], whose dopant orbitals sit close to the CBM, resulting in large orbital hybridization and modification of the CBM, and a large increase in effective mass with increased carrier concentration. In Si doped Ga_2O_3, although the dopant Si 3*s* has the same symmetry as the Ga 4*s*, the large enough energy separation between the orbitals prevents their mixing at the CBM.

Therefore, the question arises of what is the most suitable dopant among the group 14 elements to degenerately dope Ga_2O_3, that will leave the host CB edge unperturbed and provide facile addition of free electrons for high conductivity? In addition to Si, we also calculated the band structures and partial density of states of Ge and Sn doped Ga_2O_3 (80-atom supercell), as shown in Figs. 5(c) and 5(d). Because the nuclear charge of Ge and Sn is larger than that of Si, the Ge 4*s* and Sn 5*s* orbitals are expected to be energetically lower than Si 3*s* state, thus mixing more effectively with the host Ga 4*s* state at the CBM. Our calculations show that the Ge and Sn atomic contributions to the CBM state at the Γ point are 3.8% and 6.2%, respectively, much higher than that (0.8%) of Si. This is also supported by the calculated partial charge densities shown in Figs. 5(e)–5(h). At the defect states localized ∼2 eV above the CBM for Si_{Ga1} [Fig. 5(e)], the Si 3*s* orbital hybridizes with higher energy Ga and O states away from the CBM, yielding an *s*-*p* hybrid orbital shape. At the CBM, the lack of electron density observed around the Si_{Ga1} site [Fig. 5(f)] indicates that the electron density is delocalized across the lattice and there are no contributions from the Si donor states. However, considerable charge density can be seen around the Ge_{Ga1} [Fig. 5(g)] and Sn_{Ga2} [Fig. 5(h)] sites, indicating that Sn and Ge contribute states at the CBM. The large contribution of Ge 4*s* and Sn 5*s* states at the CBM changes the band dispersion at the CBM, and therefore increase the electron effective mass. This explains the lower mobility of Sn doped and Ge doped Ga_2O_3 [9–11], while a high mobility for Si doped Ga_2O_3 can be obtained even at high doping levels.

In summary, using HAXPES and hybrid DFT calculations, we explicitly determined the band-gap widening due to the Burstein-Moss shift and band-gap renormalization associated with many-body interactions in degenerately Si doped Ga_2O_3. A band-gap renormalization of as much as 0.3 eV was observed in heavily doped Ga_2O_3. The band-gap renormalization mainly results from the decrease of conduction band driven by mutual electrostatic interaction between free electrons. This is attributed to the lack of orbital mixing between the Ga 4*s* derived conduction band with the Si 3*s* dopant state. Hybrid DFT calculation reveals that the Si 3*s* state sits inside the conduction band, leaving the host conduction band edge mostly unperturbed, giving rise to a small electron effective mass. This explains the higher mobility achieved in Si doped films and suggests that Si is a superior dopant compared to Sn and Ge. Our work provides significant guidance for doping optimization of Ga_2O_3 and its use in high-power electronics and deep-UV optoelectronics.

K.H.L.Z. acknowledges funding supports from National Key Research and Development Program of China (Grant No. 2022YFB3605501) and National Natural Science Foundation of China (Grant No. 22275154). L.C. acknowledges support by the National Natural Science Foundation of China (Grant No. 51972160) and the Science and Technology Research Items of Shenzhen (Grant No. JCYJ20180504165650580). J.W. and D.O.S. acknowledge Diamond Light Source for cosponsorship of an EngD studentship on the EPSRC Centre for Doctoral Training in Molecular Modelling and Materials Science (Grant No. EP/L015862/1). D.O.S. acknowledges support from EPSRC (Grant No. EP/N01572X/1). This work used the ARCHER and ARCHER2 UK National Supercomputing Service [29], via our membership of the UK's HEC Materials Chemistry Consortium, which is funded by EPSRC (EP/L000202, EP/R029431 and EP/T022213). We are grateful to the UK Materials and Molecular Modelling Hub for computational resources (Thomas and Young), which is partially funded by EPSRC (EP/P020194/1 and EP/T022213/1). The authors acknowledge the use of the UCL Myriad, Kathleen, and Thomas High Performance Computing Facilities (Myriad@UCL, Kathleen@UCL, Thomas@UCL), and associated support services, in the completion of this work. J.W. thanks Dr. A. Regoutz for enlightening discussions. L.S.W. acknowledges the support by the National Natural Science Foundation of China (Grant No. 51771157). We are grateful to the Diamond Light Source for access to beamline I09 under Proposals No. SI24219 and No. SI31069.

APPENDIX A: THIN FILM GROWTH AND ELECTRICAL CHARACTERIZATION

Si doped Ga_2O_3 thin films were prepared by PLD using a KrF excimer laser source from respective targets on (010)-oriented Fe doped β-Ga_2O_3 substrates (Novel Crystal Technology, Japan). Si doped Ga_2O_3 targets with doping concentrations of 0.01%, 0.03%, 0.1%, 0.5%, and 1% [i.e., $Si/(Si + Ga)$] were made by mixing and grinding the appropriate proportions of Ga_2O_3 (99.999%, Alfa Aesar) and SiO_2 (99.999%, Alfa Aesar) polycrystalline powder, followed by cold pressing and sintering in air at 1350 °C for 24 h. The doping levels (x) are Si nominal values calculated from the mole ratio for the target. Before being loaded into the PLD chamber, the substrates were cleaned sequentially by acetone, isopropanol, and deionized water in ultrasonic bath for 5 min and dried by nitrogen gas. The pulsed laser with a frequency of 5 Hz was irradiated with an energy density of 1.2 J/cm^2. The film growth was carried out at a substrate temperature 600 °C with an oxygen pressure of 10 mTorr.

The temperature-dependent transport properties of the samples were characterized using a Physical Property Measurement System (PPMS, Quantum Design) in a van der Pauw four-point configuration. For all the thin films, Ohmic contact pads with a metal stack of 5 nm Ni/100 nm Au were deposited by magnetron sputtering. The contact pads were bonded through aluminum wire to the channels of the PPMS direct current resistivity puck.

APPENDIX B: HAXPES MEASUREMENTS

The HAXPES measurements were conducted at the I09 beamline of the Diamond Light Source (DLS) using a photon energy of 5920 eV. The samples were prepared by mounting the thin films on copper sample holders with carbon tape in an

electrical contact with contact pads (5 nm Ni/100 nm Au) deposited on the film surface to avoid charging effects. HAXPES spectra were measured by a VG Scienta EW4000 electron analyzer with $\pm 28^{\circ}$ angular acceptance, resulting in an overall energy resolution of 0.25 eV. The absolute binding energy scale was calibrated by an Au foil using Au's Fermi edge cutoff at 0 ± 0.02 eV and $4f_{7/2}$ core level at 84.00 ± 0.02 eV. Based on the TPP-2M method in NIST's database [30,31], the probing depth was estimated to be approximately $\sim 3\lambda$ of 22.7 nm, where $\lambda = 7.6$ nm refers to valence band electron's inelastic mean free path (IMFP).

The position of CBM, E_{CBM}, can be fitted by $a * (E_{\mathrm{CBM}} - E)^{1/4}$ where a is constant, to the feature of the CB states in Fig. 2(b). This function represents the dominant energy term in the nonparabolic conduction band density of states function and can be obtained using Kane's $\mathbf{k} \cdot \mathbf{p}$ formalism [32]. The material is assumed to be isotropic and have no crystal field splitting. Taking a useful simplifying approximation of neglecting the spin-orbit splitting (Δ_{os}) in the Ga_2O_3 [33], a two-band $\mathbf{k} \cdot \mathbf{p}$ analytic form for the conduction band dispersion can be given by

$$E_c(k) = \tfrac{1}{2}\left[-E_g + \sqrt{E_g^2 + 4k^2P^2}\right] + E_k, \tag{B1}$$

where E_g is the band gap, k is the wave vector, and P is Kane's matrix element. The P can be expressed as

$$P^2 = \frac{\hbar^2}{2m_0}\left(\frac{m_0}{m_0^*} - 1\right)E_g, \tag{B2}$$

where m_0 is the free electron mass and m_0^* is the conduction band edge effective mass. Then the density of conduction band state can be given by

$$g_c(k) = \frac{k^2}{\pi^2}\left[\frac{dE_c(k)}{dk}\right]^{-1} = \frac{k/\pi^2}{4P^2\left[E_g^2 + 4k^2P^2\right]^{-1/2} + (\hbar^2/m_0)}. \tag{B3}$$

Using the equation $E_k = \frac{\hbar^2k^2}{2m_0}$, the dominant term goes to a power of 1/4. Although this function does not use an adjustable parameter except for E_{CBM} and a scaling factor (a) to adjust the signal intensity, it has been found to best fit the conduction band dispersions of CdO in the literature [26,27].

Figure 6 show the linear extrapolation of the VB edges and the $a * (E_{\mathrm{CBM}} - E)^{1/4}$ fitting of CB states for $(Si_xGa_{1-x})_2O_3$ with different x. Since the CB filled state in the high binding energy side includes the contribution of peak tail or plasmon satellite, only the curve of CB states in the high binding energy side, representing the dominant energy term in the CB density-of-states (DOS) function, is fitted by $a * (E_{\mathrm{CBM}}\text{-}E)^{1/4}$ to determine the position of the CBM. This simulation does not use an adjustable parameter except for E_{CBM} and a scaling factor (a) to adjust the signal intensity. Even so, it reproduces the curve of CB states near the Fermi level well and gives the E_{CBM} value of 0.50 eV for 1% Si film. This value agrees well with the Burstein-Moss shift (ΔBM) 0.50 eV calculated from the carrier concentration of 1% Si film.

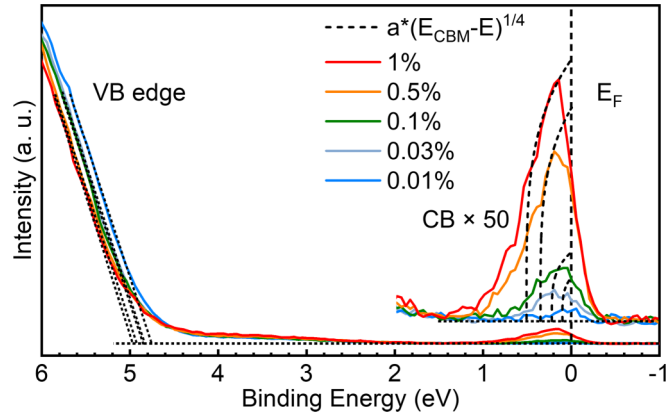

FIG. 6. The HAXPES measured top of VB and the bottom of CB regions for $(Si_xGa_{1-x})_2O_3$ with different x. The VBM positions are obtained by employing the method of linear extrapolation of the leading VB edge. Inset are the spectra magnified (×50) showing the occupied states in the CB. The $a * (E_{\mathrm{CBM}} - E)^{1/4}$ function is fitted to the feature of the CB states to estimate the CB minimum (E_{CBM}).

APPENDIX C: SEMICONDUCTOR CARRIER STATISTICS

Under the free-electron model, the Burstein-Moss shift (ΔBM) for the case of the parabolic CB is described as

$$\Delta BM = \frac{h^2k^2}{8\pi^2m_0^*}, \tag{C1}$$

where h is the Plank constant, m_0^* is the electron effective mass at the conduction band edge, and $k = (3n_e\pi^2)^{1/3}$ is the Fermi wave vector. The effective mass increases as the E_{F} is raised, and the CB curve shows nonparabolicity. The ΔBM can be corrected via an augmented version of Eq. (1):

$$\Delta BM = \frac{h^2k^2}{8\pi^2m^*}, \tag{C2}$$

where m^* is given by $m^* = m_0^*\sqrt{1 + \frac{1}{E_g}\frac{h^2k^2}{2\pi^2m_0^*}}$. Here, we used E_{g} of 4.8 eV and m_0^* of $0.28m_0$ for modeling. The carrier statistics modeled data using parabolic and nonparabolic models are as shown by solid and dashed blue lines in Fig. 4(b), respectively.

Both the electron-electron interaction (ΔE_g^{ee}) and electron-impurity interaction (ΔE_g^{ei}) are expected to induce band-gap renormalization ($\Delta \mathrm{RN} = E_g^{\mathrm{ee}} + \Delta E_g^{\mathrm{ei}}$) and compensate the ΔBM. The electron-electron interaction can be interpreted as the conduction electrons acting to screen the repulsive Coulomb interaction between conduction electrons and valence electrons. Taking the carrier concentration dependent parameter into account, ΔE_g^{ee} can be expressed as [21]

$$\Delta E_g^{ee} = \frac{e^2k^2}{2\pi^2\varepsilon_s\varepsilon_0} + \frac{e^2k_{\mathrm{TF}}}{8\pi\varepsilon_s\varepsilon_0}\left[1 - \frac{4}{\pi}\arctan\left(\frac{k}{k_{\mathrm{TF}}}\right)\right], \tag{C3}$$

where ε_s and ε_0 are static and vacuum dielectric constants, respectively, $k_{\mathrm{TF}} = 2\sqrt{k/\pi a_B^*}$ is the Thomas-Fermi screening length, and a_{B}^* is effective Bohr radius $a_{\mathrm{B}}^* = a_{\mathrm{H}}\varepsilon_s/(m_0^*/m_{\mathrm{e}})$. Here, the reported ε_s of 10.2 is used for modeling [34]. The electron-impurity interaction can be explained by the fact that the dopant atom has a larger nuclear charge than the host

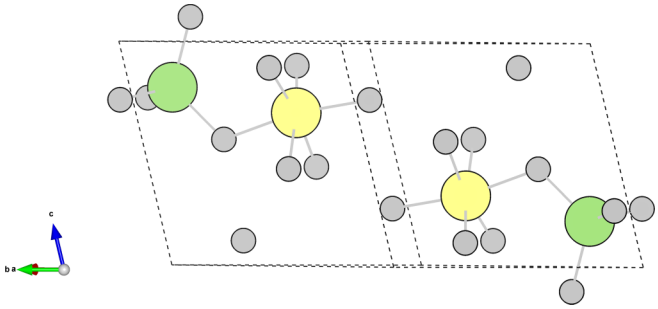

FIG. 7. Crystal structure of primitive undoped Ga_2O_3 unit cell. Symmetrically inequivalent tetrahedral and octahedral Ga sites shown in green and yellow, respectively, and O sites shown in grey.

cation, and the attractive Coulomb potential of the dopant atom causes the attractive interaction between dopant and electrons. The ΔE_g^{ei} can be expressed as [21]

$$\Delta E_g^{ei} = \frac{ne^2}{\varepsilon_s \varepsilon_0 a_B^* k_{TF}^3}. \tag{C4}$$

The modeled $\Delta RN = E_g^{ee} + \Delta E_g^{ei}$ is as shown by dash-dotted red lines in Fig. 4(c).

APPENDIX D: COMPUTATIONAL METHODS

Density functional theory calculations were performed using the periodic code VASP (version 5.4.4) [35–38], which uses a plane-wave basis set and describes the interactions between valence and core electrons using the projector augmented wave (PAW) method [39,40]. Ga[$3d^{10}4s^24p^1$], Si[$3s^23p^2$], Ge[$3d^{10}4s^24p^2$], Sn[$4d^{10}5s^25p^2$], and O[$2s^22p^4$] PAW pseudopotentials were chosen for this work. The HSE06 hybrid exchange correlation functional [41], with an increased Hartree-Fock mixing parameter α of 32%, was used in order to accurately reproduce the bulk band-gap and lattice parameters of Ga_2O_3, as has been performed in other computational studies of Ga_2O_3 in the literature [42–44]. A plane-wave cutoff of 475 eV and bulk Γ-centered k-point mesh of 8×8×4 were found to converge the total energy to less than 1 meV per atom and accurately describe the electronic structure.

The crystal structure of the β phase Ga_2O_3 contains two symmetrically inequivalent Ga cations located at tetrahedral and octahedral coordination, as shown in Fig. 7. A ten-atom supercell was used for undoped Ga_2O_3. For Si doped Ga_2O_3, two different cell sizes (80 and 180 atoms) with one Si dopant were employed to simulate different levels of Si doping in Ga_2O_3, corresponding to x doping level (and carrier concentration) of 6.3% (1.1×10^{21} cm^{-3}) and 2.8% (5.3×10^{20} cm^{-3}), respectively. For Ge and Sn doping, only the 80-atom supercell was investigated, corresponding to x doping level (and carrier concentration) of 6.3% (1.1×10^{21} cm^{-3}). Si and Ge substitutions were performed on the tetrahedral Ga site, while Sn substitution was on the octahedral site. This is in accordance with previous defect calculations on Ga_2O_3 which show a thermodynamic preference for Si, Ge, and Sn on these respective atomic positions [42]. These supercells were generated using a modify version of the PYCDT package [45]. Band structures were computed along $X(/n) \rightarrow \Gamma \rightarrow N(/n)$ depending on supercell size, and were plotted using SUMO [46]. The high symmetry point X in a primitive cell turned into $X/2$ in a doped 80-atom supercell, due to band folding arising from the halved Brillouin zone in the 2×2×2 supercell compared with the primitive cell. For the total and partial density of states for undoped and doped supercells, a Gaussian broadening of 0.6 eV and a Lorentzian broadening of 0.2 eV were applied using the software GALORE [47].

TABLE II. Lattice parameters for the conventional unit cell of β-Ga_2O_3 in this work (denoted by *) and from the literature.

Parameter	HSE06*	HSE06 lit. [43]	Experimental lit. [48]
a/Å	12.23	12.25	12.23
b/Å	3.04	3.05	3.04
c/Å	5.79	5.84	5.80
α/°	90.0	90.0	90.0
β/°	103.8	103.9	103.7
γ/°	90.0	90.0	90.0

1. Structural parameters for undoped primitive cell

The calculated structural parameters for the undoped primitive cell are summarized in Table II and show excellent agreement between theory and experiment. Small differences in lattice parameters between computational studies can be attributed to different calculation parameters being used, such as the plane-wave energy cutoff (400 eV in the study by Varley *et al.*) [43], varying amounts of Hartree-Fock exchange (32–35% across different studies) [43,49], and the inclusion (this study) or exclusion (Varley *et al.*) [43] of Ga $3d$ states as valence electrons.

2. Band structure for 1 Si dopant in 180-atom supercell

The high symmetry point X in a primitive cell became $X/3$ in the 180-atom supercell, resulting from band folding so that the length of high symmetry path along the X point to Γ point becomes a third of that in the primitive cell. In order to reduce the cost of the band structure calculation for 1 Si dopant in the 180-atom supercell, only a small section of the high symmetry path, i.e., $X/3$ point to Γ point, rather than $X/3$ point to Γ point to $N/3$ point, is selected, as shown in Fig. 8. This type of rationale has been successfully used to calculate the band structure for La doped $BaSnO_3$ [15], where only the Γ point to $M/4$ point was selected for the 320-atom supercell. Furthermore, the symmetry of the cell has been slightly reduced at the larger size, due to the relaxation of the defect. Therefore, the high symmetry point $X/3$ isn't quite at the left-hand edge of the plot, but rather about 1/5th of the way from the $X/3$ edge (see the kink in the plot). This is simply an artefact of having a defect in a large, low symmetry supercell such as Ga_2O_3 and should not affect the accuracy of the calculated band gap.

3. Density of states for undoped and doped supercells

Figure 9 shows the density of states of undoped and Si, Ge, and Sn doped Ga_2O_3 after broadening. For undoped Ga_2O_3,

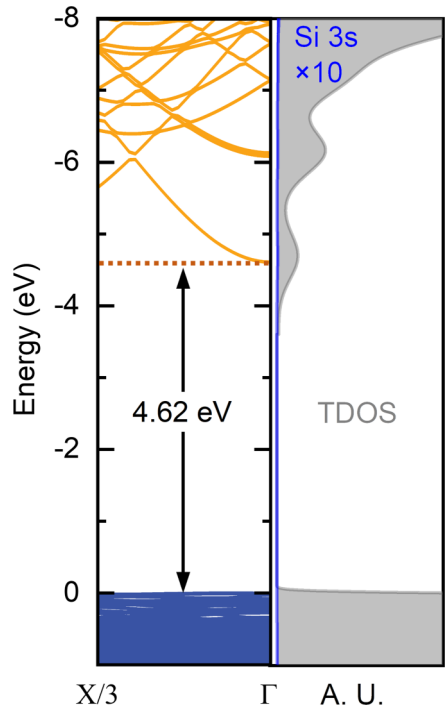

FIG. 8. Calculated band structure and total (TDOS) and partial density of states (PDOS) for 1 Si dopant in 180-atom supercell, in which the top of the VBM is set to 0 and PDOS for dopant *s* state are magnified (×10) for clarity.

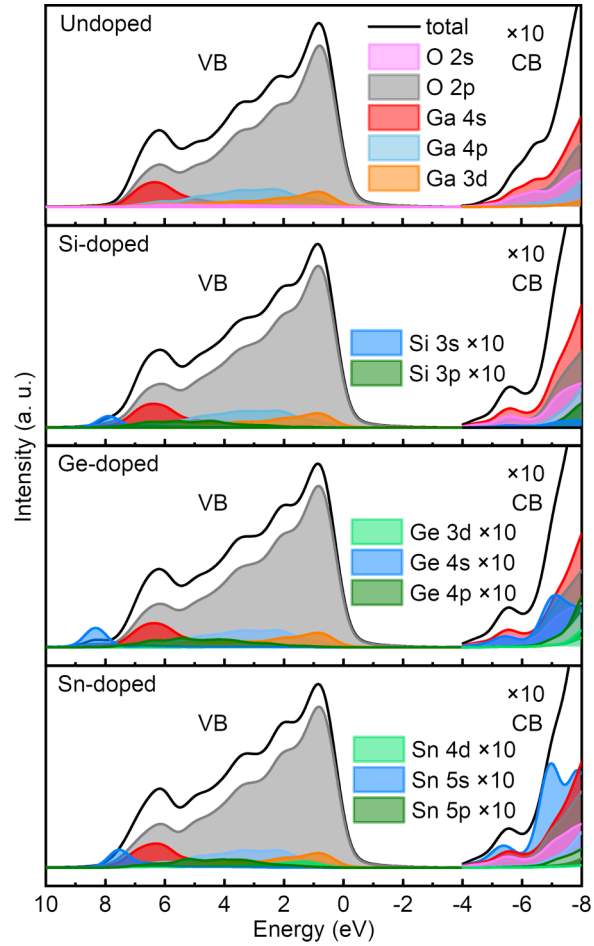

FIG. 9. Calculated total (TDOS) and partial density of states (PDOS) for all the calculated orbitals of ten-atom β-Ga_2O_3 primitive unit cell and Si, Ge, and Sn doped 80-atom supercells, in which the top of the VBM is set to 0 and PDOS for dopant *s* state is magnified (×10) for clarity.

the VBM is mainly comprised of O 2*p* orbitals that hybridize with Ga 3*d* orbitals, while the CB is dominated by the strongly overlapping Ga 4*s* orbitals, which have a favorable cross section at high photon energies. For Si doped Ga_2O_3, there is no significant contribution at the CBM (compared to the Ge and Sn CBM mixing), and a slightly increased density of Si 3*s* states at around 2 eV above the CBM (approximately at an energy of −7.5 eV). Next, we can turn to the Ge doped system, where there is a significant contribution from the Ge 4*s* donor states to the CBM. Due to the similar energy and shape of the 4*s* orbitals of Ge and Ga (neighbors in period 4), interactions between these states are strong and the CBM is significantly perturbed. Therefore, we expect poorer electron mobility in Ge doped Ga_2O_3, perhaps the poorest of the three dopants, as the dopant orbitals are most similar in Ge to the host Ga 4*s*. Finally, we can examine the Sn doped system, whose CBM has a large contribution from Sn 5*s* dopant states again due to the similar energies and shape of the Ga 4*s* and Sn 5*s* orbitals. This perturbs the conduction band minimum greatly, and again leads to lower mobility compared to Si doped Ga_2O_3.

4. Transition levels

Chemical potential limits were calculated using the the PYMATGEN PhaseDiagram module [50], and transition levels calculated using a modified version of the PYCDT [45] code and Lany-Zunger correction suite [51–54]. The transition level diagram under O-poor synthesis conditions is plotted in Fig. 10. The formation energies of the neutral defect species are summarized in Table III. We find that the Si and Ge substitutions (on the tetrahedral Ga site) are low energy shallow defects within k_BT of the CBM, while the Sn substitution (on the octahedral Ga site) is slightly higher energy and slightly further away from the CBM. This indicates that it should be possible to achieve similar carrier concentrations with Si and

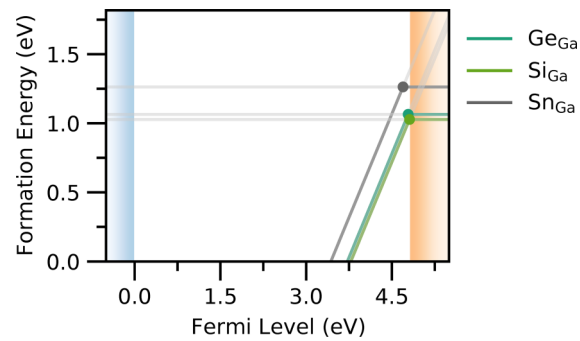

FIG. 10. Transition level diagram for Si, Ge, and Sn dopants under O-poor conditions.

TABLE III. Summary of formation energies of neutral substitution defects calculated in this work, and the formation energy reported at the conduction band minimum in the study by Varley *et al.* [42].

Species	Formation energy/eV	Formation energy (lit.) [42]/eV
Si_{Ga}	1.03	∼1.6
Ge_{Ga}	1.06	∼2.3
Sn_{Ga}	1.26	∼2.3

Ge doped Ga_2O_3 samples, while Sn may be a less effective dopant, both in terms of carrier concentration and in populating the CBM with electrons, as the transition level is further from the CBM.

The low formation energy of Si_{Ga} indicates that it is the most favorable of the three dopants examined, which is consistent with previous reports in the literature [42]. However, identification of Ge_{Ga} as another low energy species is contrary to previous work, which suggests that Ge_{Ga} (and Sn_{Ga}) both possess formation energies in excess of 2 eV. The discrepancy could result from the use of the Freysoldt correction scheme, different treatment of the neutral charge state defect, different pseudopotentials, differences in chemical potential limits (details not provided by Varley *et al.*) [42], as well as small differences in the dielectric constant and lattice parameters, or from the identification of a new, lower energy ground state defect. The significant energy differences between the two studies (over 1 eV) suggests perhaps a combination of pseudopotential effects, chemical potential limits, and the identification of a lower energy ground state.

[1] S. J. Pearton, J. Yang, P. H. Cary, F. Ren, J. Kim, M. J. Tadjer, and M. A. Mastro, Appl. Phys. Rev. **5**, 011301 (2018).

[2] J. Zhang, J. Shi, D.-C. Qi, L. Chen, and K. H. L. Zhang, APL Mater. **8**, 020906 (2020).

[3] A. J. Green, J. Speck, G. Xing, P. Moens, F. Allerstam, K. Gumaelius, T. Neyer, A. Arias-Purdue, V. Mehrotra, A. Kuramata *et al.*, APL Mater. **10**, 029201 (2022).

[4] A. T. Neal, S. Mou, R. Lopez, J. V. Li, D. B. Thomson, K. D. Chabak, and G. H. Jessen, Sci. Rep. **7**, 13218 (2017).

[5] Y. Zhang, C. Joishi, Z. Xia, M. Brenner, S. Lodha, and S. Rajan, Appl. Phys. Lett. **112**, 233503 (2018).

[6] E. G. Víllora, K. Shimamura, Y. Yoshikawa, T. Ujiie, and K. Aoki, Appl. Phys. Lett. **92**, 202120 (2008).

[7] K. D. Leedy, K. D. Chabak, V. Vasilyev, D. C. Look, J. J. Boeckl, J. L. Brown, S. E. Tetlak, A. J. Green, N. A. Moser, A. Crespo *et al.*, Appl. Phys. Lett. **111**, 012103 (2017).

[8] H. M. Jeon, K. D. Leedy, D. C. Look, C. S. Chang, D. A. Muller, S. C. Badescu, V. Vasilyev, J. L. Brown, A. J. Green, and K. D. Chabak, APL Mater. **9**, 101105 (2021).

[9] E. Ahmadi, O. S. Koksaldi, S. W. Kaun, Y. Oshima, D. B. Short, U. K. Mishra, and J. S. Speck, Appl. Phys. Express **10**, 041102 (2017).

[10] F. Alema, G. Seryogin, A. Osinsky, and A. Osinsky, APL Mater. **9**, 091102 (2021).

[11] A. Mauze, Y. Zhang, T. Itoh, E. Ahmadi, and J. S. Speck, Appl. Phys. Lett. **117**, 222102 (2020).

[12] M. Feneberg, S. Osterburg, K. Lange, C. Lidig, B. Garke, R. Goldhahn, E. Richter, C. Netzel, M. D. Neumann, N. Esser *et al.*, Phys. Rev. B **90**, 075203 (2014).

[13] A. Walsh, J. L. F. Da Silva, and S.-H. Wei, Phys. Rev. B **78**, 075211 (2008).

[14] M. Feneberg, J. Nixdorf, C. Lidig, R. Goldhahn, Z. Galazka, O. Bierwagen, and J. S. Speck, Phys. Rev. B **93**, 045203 (2016).

[15] Z. Lebens-Higgins, D. O. Scanlon, H. Paik, S. Sallis, Y. Nie, M. Uchida, N. F. Quackenbush, M. J. Wahila, G. E. Sterbinsky, D. A. Arena *et al.*, Phys. Rev. Lett. **116**, 027602 (2016).

[16] D. A. Kleinman and R. C. Miller, Phys. Rev. B **32**, 2266 (1985).

[17] S. Das Sarma, R. Jalabert, and S. R. E. Yang, Phys. Rev. B **41**, 8288 (1990).

[18] A. Chernikov, C. Ruppert, H. M. Hill, A. F. Rigosi, and T. F. Heinz, Nat. Photon. **9**, 466 (2015).

[19] F. Liu, M. E. Ziffer, K. R. Hansen, J. Wang, and X. Zhu, Phys. Rev. Lett. **122**, 246803 (2019).

[20] Z. Qiu, M. Trushin, H. Fang, I. Verzhbitskiy, S. Gao, E. Laksono, M. Yang, P. Lyu, J. Li, J. Su *et al.*, Sci. Adv. **5**, eaaw2347 (2019).

[21] K. F. Berggren and B. E. Sernelius, Phys. Rev. B **24**, 1971 (1981).

[22] B. A. D. Williamson, T. J. Featherstone, S. S. Sathasivam, J. E. N. Swallow, H. Shiel, L. A. H. Jones, M. J. Smiles, A. Regoutz, T. L. Lee, X. Xia *et al.*, Chem. Mater. **32**, 1964 (2020).

[23] J. E. N. Swallow, B. A. D. Williamson, S. Sathasivam, M. Birkett, T. J. Featherstone, P. A. E. Murgatroyd, H. J. Edwards, Z. W. Lebens-Higgins, D. A. Duncan, M. Farnworth *et al.*, Mater, Horizons **7**, 236 (2020).

[24] J. Zhang, J. Willis, Z. Yang, X. Lian, W. Chen, L.-S. Wang, X. Xu, T.-L. Lee, L. Chen, O. D. Scanlon *et al.*, Cell Rep, Phys, Sci, **3**, 100801 (2022).

[25] J. H. Scofield, in Technical Report No. UCRL-51326, Lawrence Livermore LaboratoryTechnical Report UCRL-51326, Lawrence Livermore Laboratory, 1973.

[26] P. D. C. King, T. D. Veal, and C. F. McConville, Phys. Rev. B **77**, 125305 (2008).

[27] P. C. J. Clark, A. I. Williamson, N. K. Lewis, R. Ahumada-Lazo, M. Silly, J. J. Mudd, C. F. McConville, and W. R. Flavell, Phys. Rev. B **99**, 085433 (2019).

[28] R. Cingolani, H. Kalt, and K. Ploog, Phys. Rev. B **42**, 7655 (1990).

[29] www.archer.ac.uk; www.archer2.ac.uk.

[30] S. Tanuma, C. J. Powell, and D. R. Penn, Surf. Interface Anal. **21**, 165 (1994).

[31] S. Tanuma, C. J. Powell, and D. R. Penn, Surf. Interface Anal. **43**, 689 (2011).

[32] E. O. Kane, J. Phys. Chem. Solids **1**, 249 (1957).

[33] R. Goldhahn, P. Schley, A. T. Winzer, G. Gobsch, V. Cimalla, O. Ambacher, M. Rakel, C. Cobet, N. Esser, H. Lu *et al.*, Phys. Status Solidi A **203**, 42 (2006).

[34] M. Passlack, N. E. J. Hunt, E. F. Schubert, G. J. Zydzik, M. Hong, J. P. Mannaerts, R. L. Opila, and R. J. Fischer, Appl. Phys. Lett. **64**, 2715 (1994).

[35] G. Kresse and J. Furthmuller, Phys. Rev. B **54**, 11169 (1996).

[36] G. Kresse and J. Furthmüller, Comput. Mater. Sci. **6**, 15 (1996).
[37] G. Kresse and J. Hafner, Phys. Rev. B **49**, 14251 (1994).
[38] G. Kresse and J. Hafner, Phys. Rev. B **47**, 558 (1993).
[39] P. E. Blöchl, Phys. Rev. B **50**, 17953 (1994).
[40] G. Kresse and D. Joubert, Phys. Rev. B **59**, 1758 (1999).
[41] A. V. Krukau, O. A. Vydrov, A. F. Izmaylov, and G. E. Scuseria, J. Chem. Phys. **125**, 224106 (2006).
[42] J. B. Varley, J. R. Weber, A. Janotti, and C. G. Van de Walle, Appl. Phys. Lett. **97**, 142106 (2010).
[43] H. Peelaers and C. G. Van de Walle, Phys. Status Solidi B **252**, 828 (2015).
[44] P. Deák, Q. Duy Ho, F. Seemann, B. Aradi, M. Lorke, and T. Frauenheim, Phys. Rev. B **95**, 075208 (2017).
[45] D. Broberg, B. Medasani, N. E. R. Zimmermann, G. Yu, A. Canning, M. Haranczyk, M. Asta, and G. Hautier, Comput. Phys. Commun. **226**, 165 (2018).
[46] A. M. Ganose, A. J. Jackson, and D. O. Scanlon, J. Open Source Software **3**, 717 (2018).
[47] A. J. Jackson, A. M. Ganose, A. Regoutz, R. G. Egdell, and D. O. Scanlon, J. Open Source Software **3**, 773 (2018).
[48] S. Geller, J. Chem. Phys. **33**, 676 (1960).
[49] H. Peelaers, J. L. Lyons, J. B. Varley, and C. G. Van de Walle, APL Mater. **7**, 022519 (2019).
[50] A. Jain, S. P. Ong, G. Hautier, W. Chen, W. D. Richards, S. Dacek, S. Cholia, D. Gunter, D. Skinner, G. Ceder *et al.*, APL Mater. **1**, 011002 (2013).
[51] S. Lany and A. Zunger, Phys. Rev. B **78**, 235104 (2008).
[52] S. Lany and A. Zunger, Modell. Simul. Mater. Sci. Eng. **17**, 084002 (2009).
[53] G. Makov and M. C. Payne, Phys. Rev. B **51**, 4014 (1995).
[54] S. T. Murphy and N. D. M. Hine, Phys. Rev. B **87**, 094111 (2013).